Surface temperature and the dynamics of H2 on Cu(111)
Smits, B.

Citation
Smits, B. (2023, July 4). *Surface temperature and the dynamics of H2 on Cu(111)*. Retrieved from https://hdl.handle.net/1887/3628423

Version:	Publisher's Version
License:	[Licence agreement concerning inclusion of doctoral thesis in the Institutional Repository of the University of Leiden](#)
Downloaded from:	[https://hdl.handle.net/1887/3628423](#)

Note: To cite this publication please use the final published version (if applicable).

The quantum dynamics of H$_2$ on Cu(111) at a surface temperature of 925 K: Comparing theory to experiments 2

Abstract

State-of-the-art 6D quantum dynamics simulations for the dissociative chemisorption of H$_2$ on a thermally distorted Cu(111) surface, using the static corrugation model, were analysed to produce several (experimentally available) observables. The expected error, especially important for lower reaction probabilities, was quantified using wavepackets on several different grids as well as two different analysis approaches. This allowed for more accurate results in the region where a slow reaction channel was experimentally shown to be dominant. The lowest reaction barrier sites for different thermally distorted surface slabs are shown to not just be energetically, but also geometrically, different between surface configurations. This can be used to explain several dynamical effects found when including surface temperature effects. Direct comparison of simulated time-of-flight spectra to those obtained from state-of-the-art desorption experiments showed much improved agreement compared to

the perfect lattice BOSS approach. Agreement with experimental rotational and vibrational efficacies also somewhat improved when thermally excited surfaces were included in the theoretical model. Finally, we present clear quantum effects in the rotational quadrupole alignment parameters found for the lower rotationally excited states, which underlines the importance of careful quantum dynamical analysis of this system.

6.1 Introduction

The dissociative chemisorption of hydrogen on a Cu(111) surface has, over the years, become a model system for the field of hetergeneous gas-surface catalysis, with a wide array of available experimental[1–8] and theoretical[9–24] data. In these studies the focus is on describing the elementary reaction step of the dissociation of a small molecule on a (metal) surface. These reaction steps are considered the chemically rate-limiting step in many industrial processes such as the Haber-Bosch process[25] (N_2 on Fe) or methane steam reforming[26] (CH_4 on Ni). However one of the aspects not always well described by previous studies is the effects the thermal distortion of and energy exchange with the surface have on these dissociation reactions[27, 28].

In the previous chapters, we have demonstrated that the static corrugation model (SCM) is able to accurately include all the relevant surface temperature effects for the H_2/Cu(111) system using thermally distorted, but static, surface configurations. Over the years, several other models with varying ranges of computational costs and degrees of overall accuracy have also been proposed to include surface temperature effects. For CH_4 reacting on metal surfaces Busnengo *et al.* and Jackson *et al.* reported a wide range of methods to include surface temperature effects, including sudden approximations, moving surfaces and phonon bath approaches[29–35]. Other approaches include the use of a static disorder parameter by Manson and co-workers[36], the effective Hartree potential method by Dutta *et al.*[37, 38], as well as the more general ring polymer molecular dynamics[39, 40] and high-dimensional neural network potential approaches[10, 41–43]. However, to our knowledge, the SCM is the first to have been applied in rigorous 6D quantum dynamics simulations, as introduced in Chapters 4 and 5. Nevertheless, reduced dimensionality studies have been performed in the past[44].

The SCM relies on a sudden approximation to describe the surface temperature effects of the H_2 dissociation reaction. It was designed to modify 6D perfect lattice potential energy surfaces (PESs) with an additional term that describes the change in potential energy of the surface due to thermally distorted configurations. The previous chapters have already shown that such

a static surface treatment reproduces both experiment and moving surface (quasi-)classical dynamics well, which has also been observed for methane[30]. Furthermore, the relative simplicity of the expressions used in the SCM also allow it to be used for full 6D quantum simulations of the H_2 dissociation reaction. Here we Monte-Carlo sample different (thermally distorted) surface configurations to treat the surface degrees of freedom at a quantum dynamical sudden approximation level, which has been shown to agree very well with (quasi-)classical approaches[45]. In doing so, the associated computational cost of directly adding additional surface degrees of freedom can successfully be avoided, and the possibility arises to perform (still challenging) accurate diffractive scattering calculations at low surface temperatures. These calculations can then, in the future, be directly compared to many experiments, such as the recent state-of-the-art experiments published by Chadwick *et al.* obtained using their molecular interferometry setup[8, 46]. Currently the SCM combined with surface configurations from molecular dynamics has only been used for surface temperatures of 925 K, well within the classical limit (Debye temperature) where standard molecular dynamics can be used. For low surface temperatures relevant to diffraction experiments (120 K or lower), another approach will be needed to generate the correct surface configurations adhering to Bose-Einstein statistics while avoiding the possibility of zero-point energy leaking due to the thermostat used.

Although the SCM has so far only been applied to the H_2 on Cu(111) system, its approach is expected to be general enough to be applied to other (diatomic) molecules reacting on transition metal surfaces. It is expected to perform especially well for those systems where the sudden approximation holds, i.e., where a relatively large mass mismatch between reactant and surface and short interaction times with the surface minimise energy exchange. While the effective three-body expression for the SCM coupling potential will work for any diatomic molecule interacting with a surface, new expressions would be required as the number of atoms are increased. This would be an interesting topic for future research, but is out of the scope of this thesis. The availability of a data set from for example density functional theory (DFT) calculations, which can be used to fit both the perfect lattice PES as well as the SCM coupling potential, would further reduce the workload needed to apply the SCM to other systems. Thermally distorted surface configurations can be obtained for cases well within the classical limit using a variety of force-field methods, such as the embedded atom method that we employ for this thesis. These surface configurations can also be approximated using, for example, the Debye-Waller factor as was done in the earlier SCM studies[19, 24].

Chapter 5 demonstrated that the SCM reproduces experimental dissociation

probabilities well for the lower energy ranges at both the quantum and the quasi-classical level. Nevertheless, it also shows that direct comparisons to experimentally fitted dissociation curves is difficult across the entire energy range, due to the uncertainties in the available experimental data[16]. Therefore this chapter will focus on several observables which can be derived from earlier results, supplemented with some additional calculations where needed. We will discuss the effect of the time step on our QD simulations, especially at very low reaction probabilities, and the accuracy that is expected from the methods employed. These results can then be used to investigate the presence or absence of an experimentally observed slow reaction channel in more depth, which was previously left an open question due to the compromise between accuracy and computational cost that had been made. We present several 2D cuts of the PES for different thermally distorted surfaces, and show how the thermal displacement of surface atoms changes not only the lowest barrier heights, but also their geometry on the 2D cut. Next we discuss several fits to the dissociation probability curves that were obtained, comparing fit parameters to those obtained from the experiments. We also use these fits to obtain simulated time-of-flight spectra, which should allow for a more direct comparison of experimental associative desorption results. Finally, we present results on the effect of the internal energies of the H_2 on the dissociation reaction, using both rotational and vibrational efficacies and the rotational quadrupole alignment parameter. Overall, we hope the results presented here will provide a solid data set for future comparative experimental and theoretical work.

6.2   Methods

Previous chapters focused on dissociation and (rovibrationally elastic) scattering probabilities obtained using either the EAM-SCM or the BOSS PESs, both at a QD and a QCD level. Here we will instead compare other variables and/or observables that can be obtained from these probability curves. Thus the results presented in this chapter will be almost directly based on those presented in Chapters 4 and 5, with some additional data added where needed.

6.2.1   Quantum dynamics

We expand on the available QD results of the previous chapters by adding a WP in the 0.95-1.50 eV energy range for the results in the initial vibrational ground state. Also included is the WP in the 0.65-1.00 eV range for the v=1, J=1 states. For the initially rotationally excited states, only those states with $m_J \geq 0$ were considered, with the results for $m_J \neq 0$ counted twice in the total

average per rotational (J) state. This double counting accounts for the $m_J < 0$ states (as R_{v,J,m_J} should equal $R_{v,J,-m_J}$).

We propagate our WPs using the split operator (SPO) method,

$$\Psi(\overrightarrow{Q};t_0 + \Delta t) = \quad \exp(-\frac{i}{2}K\Delta t) \cdot \exp(-iV(\overrightarrow{Q})\Delta t) \qquad (6.1)$$
$$\exp(-\frac{i}{2}K\Delta t) \cdot \Psi(\overrightarrow{Q};t_0) + O[(\Delta t)^3],$$

with K being the kinetic energy part of our Hamiltonian, as implemented in our in-house code[45], and further discussed in section 2.1.3 of Chapter 2. Here the WPs are propagated in a stepwise fashion, first taking a half-step for the free particle propagation, then a full time step action of the potential is applied, followed by another half-step as a free particle. This stepwise propagation method inherently results in an error $O[(\Delta t)^3]$ that scales with the size of the time step used.

We use a quadratic form of the optical potentials in the scattering and reactive channel regions[47]. The scattered fraction is analyzed through the scattering matrix formalism[48], which yields the scattering probabilities for each rovibrational state and diffraction channel separately. The sticking probability is subsequently calculated by subtracting the sum of all these scattering probabilities from one. For some simulations, these sticking probabilities are also compared to those obtained from a flux analysis in r[49, 50]. This approach directly measures the flux through a plane for a specific large enough value of r, but does not yield any information on the scattered states. For a more in-depth discussion of the basis of these quantum mechanical methods, we direct the reader to section 2.1 of Chapter 2.

Only those thermally distorted surface atoms in the top two layers of the surface slab, and within the SCM cutoff distance of 16 bohrs (~ 8.47 Å) of the 1×1 unit cell corner, are included in the SCM, as this is where the coupling potential is available[24]. To obtain a single representative dissociation curve for H_2 reacting with thermally distorted Cu(111) at a QD level, we average the probabilities obtained for a total of 104 unique thermally distorted surface slabs. Chapter 4 showed 104 surfaces was enough to reproduce the results of including the full dataset of 25000 surface configurations with only a small error.

6.2.2   Rotational quadrupole alignment parameter

The rotational quadrupole alignment parameter $[A_0^{(2)}(J)]$ is a measure of preference for the H_2 to dissociate in particular m_J states. When it is positive,

dissociating molecules prefer to react rotating parallel to the surface ($|m_J| = $ J; "helicopter"), while negative values indicate a preference for reactionof molecules with a rotation perpendicular to the surface ($|m_J| = 0$; "cartwheel"). A value of zero indicates no preference for either.

The rotational quadrupole alignment parameter (RQAP) is defined as

$$A_0^{(2)} \equiv \langle 3\cos^2\theta_L - 1 \rangle \tag{6.2}$$

with θ_L the angle between the angular momentum vector and the surface normal. The RQAP can also be computed through

$$A_0^{(2)}(J; v) = \frac{\sum_{m_J} P_{stick}(v, J, m_J)\left(\frac{3m_J^2}{J(J+1)} - 1\right)}{\sum_{m_J} P_{stick}(v, J, m_J)}, \tag{6.3}$$

with $P_{stick}(v, J, m_J)$ the sticking probabilities for the specific rovibrational state. Assuming using associative desorption detailed balance the RQAP can also be measured experimentally, although there are no studies available for the H$_2$ on Cu(111) system to our knowledge. However, some data for D$_2$ is available[5, 51, 52].

6.2.3 Simulating time-of-flight spectra

To more directly compare to the time-of-flight (ToF) spectra obtained from the state-selective desorption experiments, we can also directly simulate ToF spectra from our dissociation curves, as described in section 2.4.2 of Chapter 2. In short, the experimental approach of Ref. [2] is mirrored, making use of direct inversion under the assumption of detailed balance to directly relate the dissociative adsorption results to the ToF spectra obtained from associative desorption. The intensity of the ToF spectrum is related to the sticking probability function multiplied by a flux-weighted velocity distribution expressed in the time domain,

$$I(t')dt' = K \cdot C(t') \cdot \exp\left(\frac{-E_{kin}[t']}{2k_bT_s}\right)\left(\frac{x_0}{t'}\right)^4 \cdot P_{stick}(E_{kin}[t'])\,dt' \tag{6.4}$$

with k_b the Boltzmann constant, T_s the surface temperature, K a proportionality constant, $E_{kin} = m\left(\frac{x_0}{t'}\right)^2$, and $t' = t - t_{shift}$. t and t_{shift} describe the travel time in and after leaving the field-free region, respectively, and x_0 describes the length of this field-free region in the detector of the experimental setup that is being simulated.

The cutoff function we used was of an exponential form

$$C(E_{kin}) = 1 - e^{-E_{slope}(E_{kin}-E_{min})} \text{ for } E_{kin} > E_{min}, \qquad (6.5)$$

based on the kinetic energy of the molecule, as was obtained in the experimental study[7]. The cutoff parameters E_{slope}, which governs how fast the signal decays, and E_{min}, which determines the minimal energy the molecule needed to be experimentally detectable, were obtained from the same experimental study.

The dissociation curves were fitted to the error function (ERF), Gompertz function (GMP), and the five-parameter function (FPC) forms to obtain a continuous representation of $[P_{stick}(E_n)]$. These continuous representations are required to accurately apply (6.4) over the entire time range. Both the QD and QCD results were fitted to these functional forms using a Levenberg-Marquardt routine, minimising the residual difference between the available data-points and the model. For those QD results where there is overlap between the different WPs at the same energy, the WP reaching up to higher energy was always chosen to prevent double counting during the fitting procedure. Using the lower energy WP, however, should work equally well.

6.2.4 Threshold offset and efficacies

Using the state-selective results, rotational and vibrational efficacies can also be obtained. These in particular indicate the ability of the rotational and the vibrational energy of H_2 to promote reaction with the surface, which is an often available from experiments. In this chapter the method by Shuai *et al.* is used[53], which relies on first finding the energy offset between the rotational or vibrational ground state and each specific curve. This approach also gives another observable, in the form of the threshold offset itself, to compare to, as described in section 2.4.3 of Chapter 2.

For this chapter, the difference between the logarithms of the two reaction curves was also minimised to obtain the threshold offset, similar to the procedure in Ref. [7]. Although using the logarithm of the results should put a focus on the curve onset of the dissociation curves, it did not appear to change the final results significantly.

6.3 Results and Discussion

6.3.1 Effect of QD time step

In Chapter 5, we discuss an unphysical "upturn" present for the QD results at very low reaction and energy, which appears within the same range as the
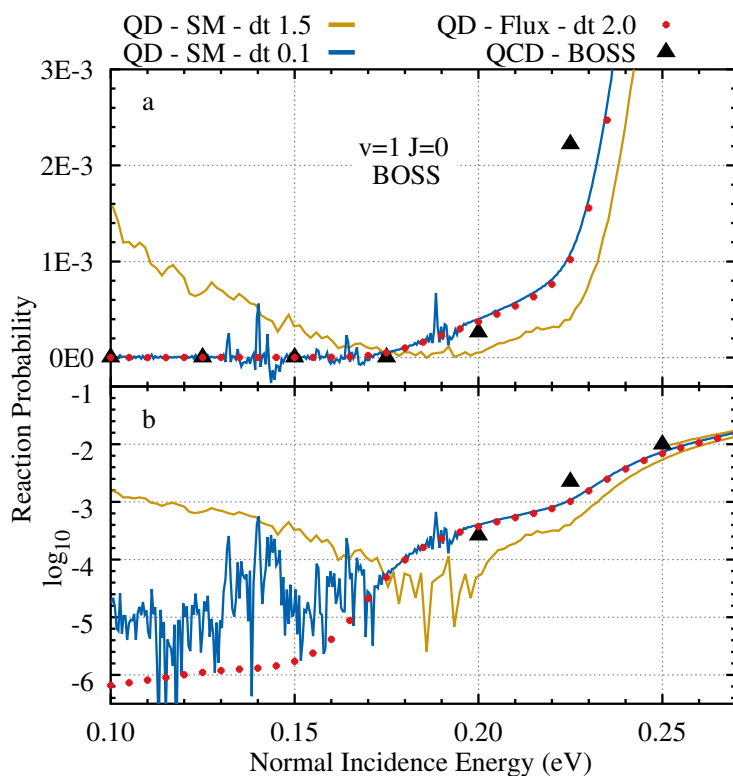
6

FIGURE 6.1: Dissociative chemisorption probabilities of H_2 on Cu(111) for the first vibrationally excited state, obtained using the BOSS approach and several different time steps. Included are: (orange) QD results for a time step of 1.5 au using the scattering amplitude formalism, (blue) QD results for a time step of 0.1 au using the scattering amplitude formalism, (red circles) QD results for a time step of 2.0 au using flux analysis method, and (black triangle) QCD results. Both a regular (a) and a logarithmic (b) scale are used for the reaction probabilities.

experimental "slow" channel fitted by Kaufmann *et al.*[7]. However, its shape led us to believe it was more likely to be noise due to the split-operator method (Eq. 2.31) being used with a too large time step, this method having an inherent error scaling with $O(\Delta t^3)$. Other parameters of the QD calculation, such the size of the specular and scattering grid, the distance of the analysis plane from the optical potential, and the parameters governing the optimal absorption of these optical potentials, were found to have little to no effect on the magnitude of this noise.

To verify the upturn found in the previous study and investigate the influence of the propagation time step, we now compare our previous results to new QD results obtained with a time step of 0.1 au (vs. 1.5 au for our original calculations), as is shown in Figure 6.1. Next to these small time step (blue) and larger time step (orange) curves, we also include the QCD-BOSS results in black and the results of the flux analysis method on the same system and a time step for propagation of 2.0 au.

Comparing the computed reaction probabilities on the regular [Fig. 6.1(a)] and the logarithmic [Fig. 6.1(b)] scale, we clearly see this "upturn" for the larger time step results obtained with the scattering amplitude formalism (SAF), resulting in an error in the range of 10^{-3}. In contrast, the flux analysis method appears to converge to much smaller probabilities in the 10^{-6} range, even with a larger time step for propagation. It should, however, be noted that this analysis method only yields reaction probabilities, and is thus not suitable to obtain rotationally and vibrationally (in)elastic scattering probabilities. Finally, by much reducing the time step, we are able to reduce our error in the results of the SAF to the range of 10^{-5}, as can be seen by the blue curve. Interestingly, this smaller time step also has some effect on the higher energy ranges just above the threshold for reaction, slightly reducing the reaction probabilities we find similarly to how they are increased at low energy. The good agreement between flux analysis and SAF results does appear to indicate we obtain accurate reaction probabilities to as low as $10^{-4.5}$ (around 0.17 eV of incidence energy), where the flux analysis and SAF results diverge.

Different noise-like peaks, most notable around 0.140, 0.165, and 0.190 eV, have also become more apparent for the QD results obtained with the smaller time step. These peaks are attributed to entrance channel resonances, i.e., trapping of the molecule due to an excitation of the molecular bond as it is weakened near the surface. Due to the use of the SAF this trapping results in a small increase in reaction probability, as has also been observed with much earlier implementations of this analysis method[54, 55]. While we do not expect these resonances to become much more important as the time step is decreased, we do expect the error they introduce to become more relevant as other sources

of noise are reduced. As the flux analysis method only analyses the reactive flux it is insensitive to this trapping.

Overall, these results once again underline the importance of carefully crafted wavepackets when using the SPO method, but also give us a range of error we can expect when further analysing the results for this, and previous, studies. Clearly, as in every computational study, one always needs to balance accuracy and computational cost as reducing the time step from 1.5 to 0.1 au makes every single WP calculation, of the 104 we need to perform per energy range when including the SCM, 15 times more expensive. Such a study would thus be more than 1500 times more expensive than a traditional 6D BOSS QD WP calculation, which nowadays takes roughly 24h on a modern 32 core CPU.

Although the balance between accuracy and computational speed of the SPO method is very favourable for most of the calculations we performed in this work, for these curve onsets (and perhaps for other systems in general) the method scales poorly for lower time steps. Therefore another approach could be to instead implement another propagation method, which might not perform as computationally efficient for higher reaction probabilities but does yield significantly lower propagation errors[56]. Comparisons between the different propagation methods when applied to our system would also allow for a clearer estimate of the error we find for the SPO propagation, regardless of the final analysis method used. Nonetheless, it is noted that for probabilities at the threshold and beyond, the usual accuracy of 10^{-3} using dt = 1.5 au is quite sufficient.

6.3.2   Barrier shape and location

Next we will first discuss several cuts of the PES and the location of the transition state found there, both for thermally distorted surfaces and the perfect crystal. These cuts will shed some light not only on the changes in lowest barrier heights brought about by including the SCM but also demonstrate how the location of the barrier can change as the surface atoms are shifted from their ideal lattice positions. These slabs were obtained from the dataset of surfaces generated in Chapter 3 through molecular dynamics at a surface temperature of 925 K, applying a highly accurate EAM potential[59]. In Fig. 6.2 and Fig. 6.3, we present a collection of two sets of contour plots (or elbow plots) of the PES at the (lowest barrier) bridge-to-hollow (bth), and the top-to-fcc (ttf) reaction sites, respectively. Generally, these lowest barrier sites will have major effects on the shape of the dissociation curves, as they provide a predictive tool for the onset of the reaction. In panels (b), (c), and (d) of Figs. 6.2 and 6.3, we show the potential for a specific less reactive, a very
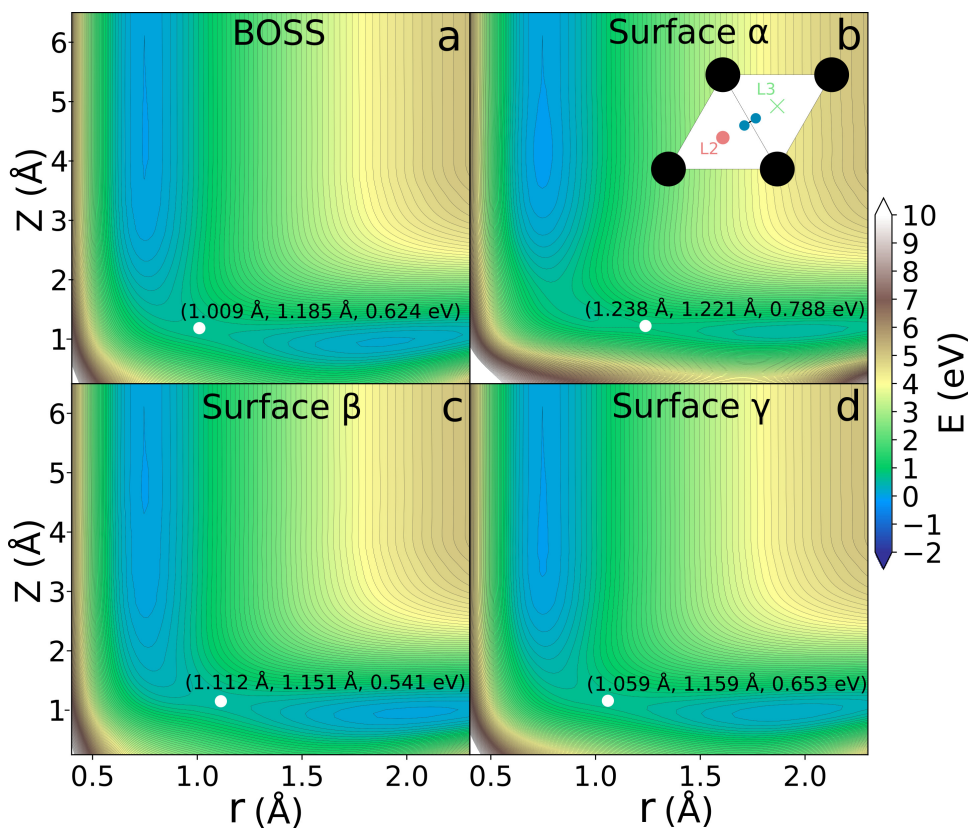
FIGURE 6.2: Potential energy contour plot for the bridge-to-hollow (bth) reaction site, as depicted in panel b. The PES was interpolated using the CRP[57] using DFT obtained with the SRP48 functional[22, 58]. Included are the potential for the (a) BOSS approach, as well as three different SCM distorted surfaces: (b) less reactive α, (c) very reactive β, and (d) typical reactivity γ, which have also been discussed in Chapter 4. The transition state for each 2D PES is marked with a white circle, including the location of the barrier in the (r, Z, V) format. The distorted surface slabs for the SCM, at a modelled surface temperature of 925 K, were obtained from Chapter 3.
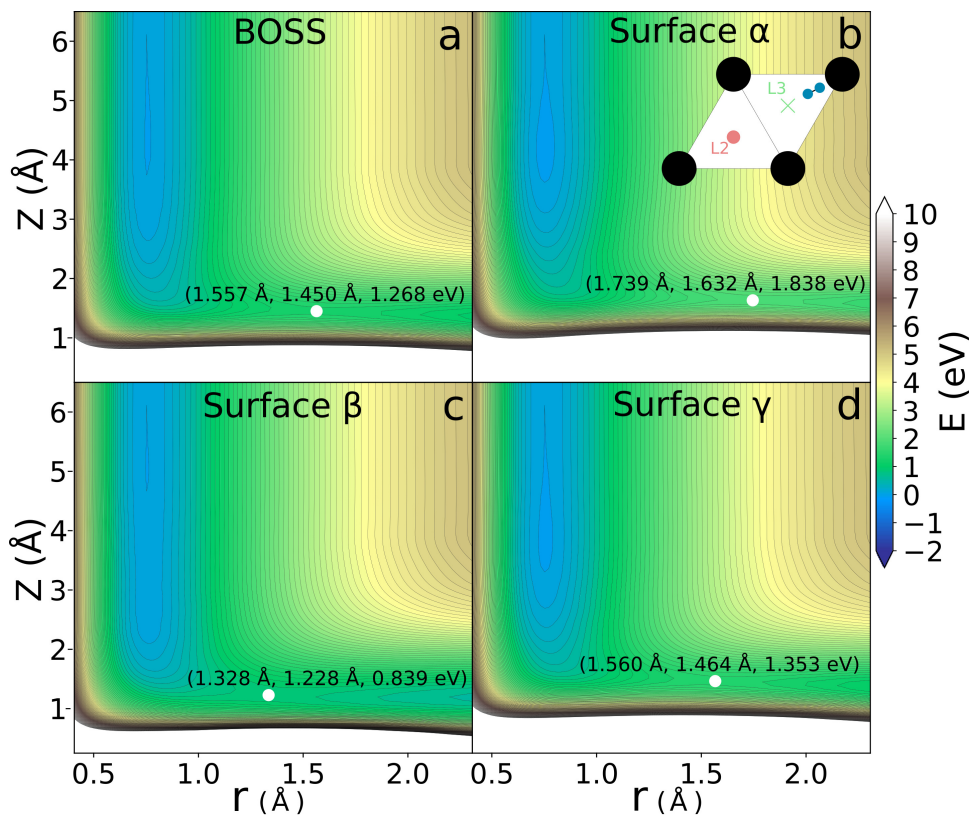
FIGURE 6.3:   Potential energy contour plot for the top-to-fcc (ttf) reaction site, as depicted in panel b. The PES was interpolated using the CRP[57] using DFT obtained with the SRP48 functional[22, 58]. Included are the potential for the (a) BOSS approach, as well as three different SCM distorted surfaces: (b) less reactive α, (c) very reactive β, and (d) typical reactivity γ, which have also been discussed in Chapter 4. The transition state for each 2D PES is marked with a white circle, including the location of the barrier in the (r, Z, V) format. The distorted surface slabs for the SCM, at a modelled surface temperature of 925 K, were obtained from Chapter 3.

reactive, and a typically reactive surface slab respectively, while the transition state location is also marked in the (r, Z, V) format for each of these cuts. The ttf reaction site was included specifically due to the large differences in barrier height between the surface slabs we discuss. These same three surface slabs have also previously been discussed in Chapter 4, where their associated reaction and (rovibrationally elastic) scattering probabilities are shown.

Of particular note is the shift of the lowest reaction barrier, both in r and in Z, when the surface is thermally displaced. This shift can have further dynamical effects also on the contribution of rovibrational energies to the dissociation reaction, as we will show in the next sections. Previous studies have already carefully characterised the effect of individual surface atom displacements, both parallel and normal to the surface, on the barrier height and location[18, 21]. Now we also show how all these effects work together to form a very different potential energy landscape between different thermally distorted surfaces. For the (lowest barrier) bth PES cuts (Fig. 6.2) we find that the inclusion of surface temperature effects shifts the location of the reaction barrier toward higher H−H distances, while also slightly moving this barrier closer towards the surface. In contrast, for the lowest reaction barriers of the ttf PES cuts (Fig. 6.3) we find barriers with much lower (higher) r and Z values for the very reactive (non-reactive) surface slab we included. However, even the most reactive barrier here is much higher than the barriers found for the bth site, and is thus more important for higher ends of the dissociation curves. We would, however, also note that this is only a very small part of the dataset of 25.000 distorted surface configurations used in this work, as each distorted surface slab will have a uniquely shaped potential energy landscape.

6.3.3 Time-of-flight spectra and fitted parameters

To get a more direct comparison to the available results of associative desorption experiments, we have simulated time-of-flight spectra for each of our dissociation curves. Here, we rely on detailed balance and several parameters of the experimenal setup by Kaufmann *et al.* to allow for the best possible comparisons to their results. As the experimental setup was recalibrated every day between measurements, we chose a constant time offset ($t_{shift} = 3.2 \ \mu$s) and the length of the field-free region ($x_0 = 29.25$ mm) for Eq. 6.4 as was reported in Ref. [7]. For the continuous expression of the dissociation curve, we use the GMP for the v = 0 QD-BOSS and all QD-SCM results, and the FPC for the v = 1 QD-BOSS and all QCD results.

As advised by the experimentalists in private communication, it was also decided to simulate the experimental ToF spectra using their published ERF
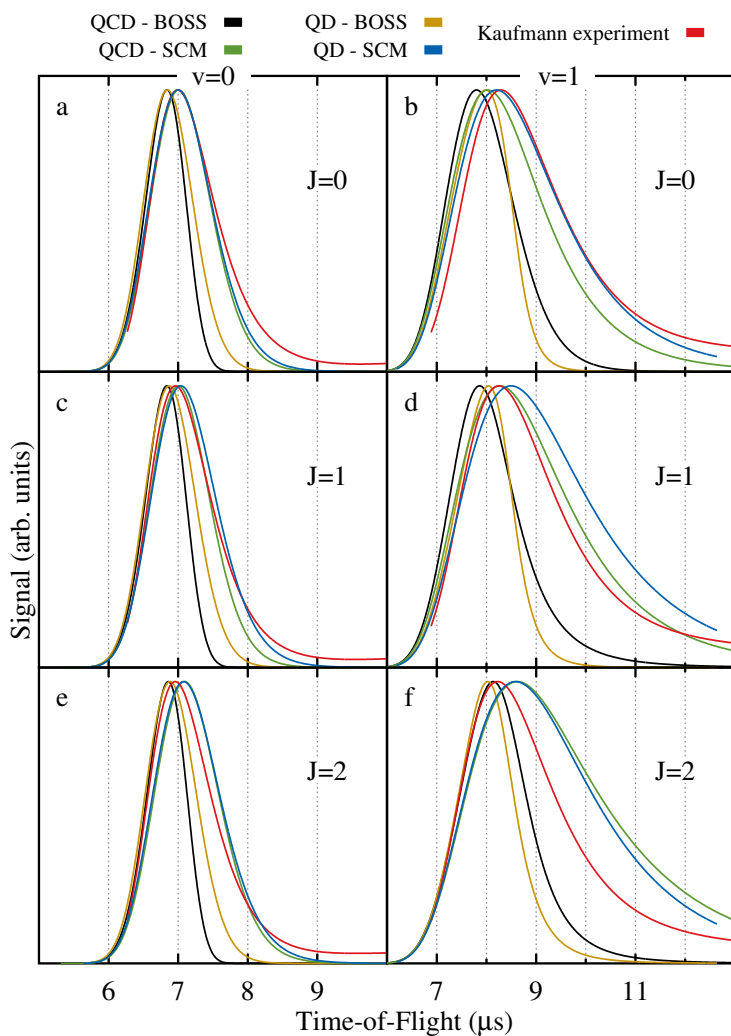
FIGURE 6.4:   Simulated time-of-flight spectra for six rovibrational states: v = 0, [(a), (c), and (e)] J = 0, 1, 2 and v = 1, [(b), (d), and (f)] J = 0, 1, 2. Spectra are generated using fits to the QD-SCM (blue), QCD-SCM (green), QD-BOSS (orange), and QCD-BOSS (black) dissociation curves, and fit to the GMP or FPC functional forms. Parts of these dissociation curves are also shown in Chapter 5, Also included are the experimental results by Kaufmann *et al.*[7], simulated using the published ERF function fits including the slow channel. A surface temperature of 925 and 923 K was used for the theoretical and experimental simulation, respectively.

paramters. This should allow for a more direct comparison of the theoretical results to the experimental curves. The cutoff function of equation 6.5 was used for the simulation of both the experimental and the theoretical spectra, with $E_{slope} = 22.8$ eV^{-1} and $E_{min} = 7.2$ meV, using values typically reported by Kaufmann *et al.*[7] Finally, we used a modeled surface temperature of 923 and 925 K for the experimental and theoretical results respectively. Although using only an average of the ToF simulation parameters reduces our ability to directly compare to the experimental results as they were recorded, we believe it will also reduce the error we can expect due to the needed daily calibrations. Similarly, we expect little data to be lost by simulating the experimental spectra from the ERF fits, as they have been shown to be very accurate by the experimentalists[7].

In Fig. 6.4 we present the simulated ToF spectra for several rovibrational states, both for QD- and QCD-SCM and -BOSS results, compared to the simulated experimental results of Kaufmann *et al.* Of note is the broadening of the SCM results when compared to the BOSS spectra, which we attribute to the characteristic curve broadening effect due to surface temperature[60]. Here the lower reaction barrier of some surface configurations improves dissociation, while unfavourable configurations (as well as a recoil effect[61]) reduce reactivity at higher energies. Peak locations found for the SCM are similarly found at a slightly longer ToF compared to the BOSS. We also find good agreement between the QD and QCD results, although some differences are found for the vibrationally excited states, similar to what is observed for the dissociation curves themselves (Chapter 6). In general, the SCM does increase agreement with the experimental spectra for all states, although it appears to perform much better for the vibrational ground states. For the rovibrationally excited states, the SCM appears to somewhat overestimate the widths of the curves.

The theoretical dissociation curves were also fitted to the ERF functional form, described in more detail in section 2.4.2 of Chapter 2. The three fitting parameters obtained for the QD- and QCD-SCM and -BOSS fits are presented in Fig. 6.5 and compared to those obtained from experiment.

While these fits are commonly used to efficiently compare dissociation curves, we also find the ERF functional form performs the worst, of the functional forms we tried, in accurately describing our obtained results from the QD and QCD. Furthermore, studies have shown that the three fitting parameters E_0, W, and A are not fully independent of each other[3, 19]. Nevertheless, some information can be gained by comparing these fitted parameters directly. Experimental saturation values (A) were not included, as they cannot be directly obtained from the desorption experiments, while the experimental width parameters (W) were only reported as a constant value per vibrational state.
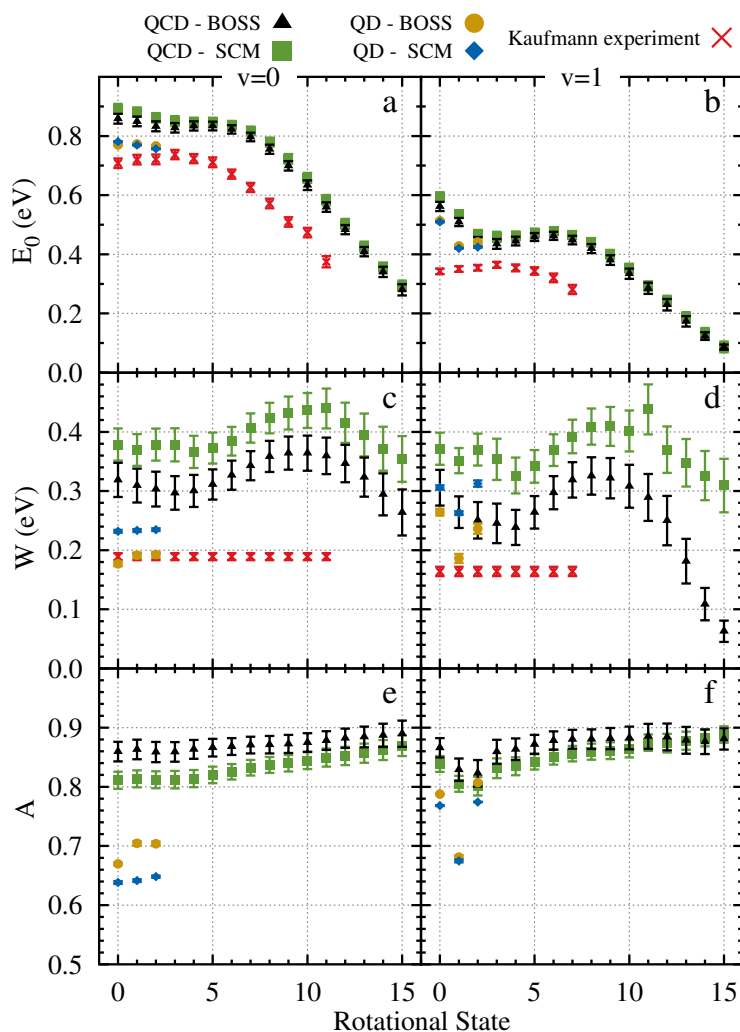
FIGURE 6.5: Fitted ERF parameters for the fits to the QD-SCM (blue), QCD-SCM (green), QD-BOSS (orange), and QCD-BOSS (black) dissociation curves, for the [(a), (c), and (e)] v = 0 and [(b), (d), and (f)] v = 1 vibrational states, plotted against the rotational (J) state. Included are the: [(a) and (b)] E_0, [(c) and (d)] W, and [(e) and (f)] A parameters, as shown in (2.70) of Chapter 2. Where available, the experimental results of Kaufmann *et al.*[7] are also included. Error bars represent a standard deviation of 2σ, obtained from the fitting procedure.

We observe a slight difference between the E_0 parameters [Fig. 6.5(a),(b)] of the BOSS and SCM approaches, both at the QD and the QCD level. Those parameters found when fitting the QD results are however somewhat lower in energy, more so for the vibrational ground state (a) than the vibrationally excited state (b). The experimental fits yielded even lower values, although qualitatively theory appears to generally predict the right shape as the rotational state increases, where reaction occurs earlier as the rotational energy increases. Only at the lowest rotational states do we see small qualitative differences, where the experiment predicts a small increase in E_0, which theory only finds later around $J = 5$.

For the curve widths (W) [Fig. 6.5(c) and (d)], we see a similar split between experiment and theory, where both the SCM and BOSS predict higher widths than found for the experimental fits. Both the QD- and QCD-SCM results show a higher curve width than the matching QD- and QCD-BOSS results, as is characteristic for surface temperature effects. Focusing on the QCD widths, we see that they generally very slowly decrease as the rotational state increases, which we can attribute to the additional rotational energy helping the molecule pass the barrier without opening up new reaction paths at higher barriers. At higher rotation, the new increase in width could indicate the opening up of later (in r) reaction pathways, which are more efficiently surpassed for molecules with a higher rotational state. This can be understood by the scaling of $\frac{1}{r^2}$ as found in Eq. 2.9. As r increases, the rotational energy of the molecule must decrease to ensure conservation of angular momentum as it approaches the barrier and does not change state. This rotational energy can thus assist in surpassing the dissociation barrier[62]. Finally, at very high J-states even these later barriers are easily passed by the very high (rotational) energy of the molecule, and widths rapidly decrease again. Especially for the vibrationally excited states, this decrease is likely due to the internal energy of the molecule being high enough to allow for the dissociation to occur, even without any significant kinetic energy towards the surface.

It is known that for H_2 on Cu, the vibrational energy can assist in promoting the reaction, which we also discuss in section 6.3.4. Somewhat similar effects were observed in one of the earliest studies using the SCM, however here the decrease in width for the higher (rotational) states was much less apparent[19]. Unfortunately, not enough rotational states have been calculated to attempt a similar analysis for the QD results, and the experimental results were only fitted to a single width per vibrational state.

For the saturation values (A) [Fig. 6.5(e) and (f)] we find that the BOSS approach generally predicts slightly higher values than the SCM, although this difference decreases as the internal energy of the molecule increases. This can

be well explained by a change in barrier heights, locations, and/or the potential energy landscape surrounding these barriers, when considering different surface configurations, which we show to have a major effect (see section 6.3.2). Here, some non-reactive configurations will simply have no clear reaction path on some higher barrier regions of the full potential. These specific surface slabs would then be much less reactive, decreasing the maximum reaction probabilities that are obtained when sampling many configurations.

A also increases very slowly as the internal energy goes up, which can be explained easily by even the highest reaction barriers being more easily overcome in the incidence energy ranges we investigated. The values for the (QCD-)SCM approach increase slightly faster, likely due to the much larger collection of different barriers available due to all the different surface configurations. It is not exactly clear what causes the dip in saturation value around the J = 1 for the vibrationally excited states. Perhaps the low rotational energy combined with the excited vibrational state prevents the molecule from easily surpassing the reaction barrier due to unfavourable rotational angles. In contrast, for the rotational ground state there would be no (significant) rotation to have any effect, while for higher states the much higher rotational energy can more easily facilitate reaction purely energetically.

QD results predict a lower saturation than those obtained with QCD, slightly closer to those predicted by some experimental studies, although it is unclear what could cause this difference. It could be simply related to the fact that energy can be far more easily converted between degrees of freedom in QCD when compared to QD. For QD the molecule cannot as easily convert its quantised internal energy into degrees of freedom related to the reaction path, at least when compared to the classical nature of the QCD.

6.3.4   Rotational and vibrational efficacies

The "threshold offset" parameter (ΔS) will give us an indication of the increase in reaction probability due to the additional internal energy of higher rovibrational states. It is represented by the energy shift that gives the optimal overlap between the results of the rovibrational ground state and the rovibrationally excited states (see Eq. 2.74 of Chapter 2). As was suggested by previous studies, we can use ΔS to determine how efficiently the internal rotational (Eq. 2.75) and vibrational (Eq. 2.76) energies promote the dissociation reaction in a way that is more independent from the functional form chosen when fitting the dissociation curves. Indeed, we find negligible differences in ΔS when obtained from fits to different sigmoid functions (ERF, GMP, and FPC) or even using the raw results directly.
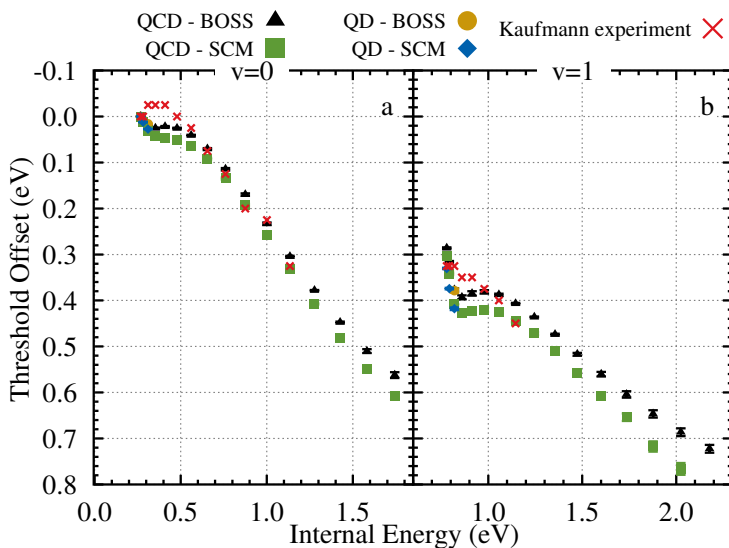
FIGURE 6.6: Threshold offset parameters for the QD-SCM (blue), QCD-SCM (green), QD-BOSS (orange), and QCD-BOSS (black) dissociation curves, for the (a) v = 0 and (b) v = 1 vibrational states, plotted against the total internal (rovibrational) energy of the H_2 molecule. Internal energies are obtained from the FGH method for the SRP48 PES. Where available, the experimental results of Kaufmann *et al.*[7] are also included. Errorbars represent a standard deviation of 2σ, obtained from the fitting procedure.

In Fig. 6.6, we compare the obtained threshold offsets for the vibrational ground state (a) and vibrational excited state (b), plotted for each rovibrational internal energy (obtained from the FGH method). In contrast to experiment, we do not find small negative ΔS values for very low rotational states of the vibrational ground state. Instead, we see a rapid increase in offset value, followed by a small region of constant shift around J = 5, which is especially noticeable for the v = 1 results. This observation is also reflected in the similar behaviour of the E_0 parameters presented in Fig. 6.5. For the higher internal energies, at higher rotational states, we see both theory and experiment move towards a linear section. Interestingly the QCD-SCM results appear to increase slightly more rapidly compared to the QCD-BOSS results, which is more obvious for the v=1 states in Fig. 6.6(b). This more rapid increase, combined with the generally higher values found for the SCM results, would indicate that the internal energy of the H_2 molecule can be more easily used to surpass the dissociation barrier of the thermally distorted surfaces compared to the perfect crystal lattice. This observation could be explained by the much more varied number of barriers encountered on the distorted surfaces, and their sensitivity to different rovibrational energies. The agreement between the QCD and QD results appears to be excellent, although little can be concluded of the shape of the full range of internal energy due to the limited amount of QD data available.

The rotational efficacies in Fig. 6.7. show the expected trends based on these threshold offsets. The differences between the theory and experiment, however, are much more pronounced as the rotational energies are in the same order of magnitude as the threshold offsets when considering the lower rotational states. Due to these smaller energies, we also expect there to be larger errors present both in the theoretical and experimental results. Nevertheless, we do expect the basic trends we describe, and the comparisons between the purely theoretically obtained results below, to be accurate enough. For the low rotational states, experiments predict a negative rotational efficacy, where rotation actually hinders the dissociation reaction, known as "rotational cooling"[3] In contrast, our theoretical results fail to predict this cooling, instead showing a very efficient use of rotational energy to pass the reaction barrier. For the vibrationally excited states in panel (b), we even find efficacies above 1, which would indicate 1 meV of rotational energy would help passing over more than 1 meV of reaction barrier. This then would be well explained by very late reaction barriers, where rotational energy can greatly contribute to the dissociation reaction. QD- and QCD-SCM efficacies appear to be slightly higher than those found for the BOSS results, which again indicates the rotational energy can be more efficiently used to pass the barrier at low J-states. This observation matches well with the later barriers (in r) we find in Fig. 6.2. Nevertheless, the SCM, BOSS, as
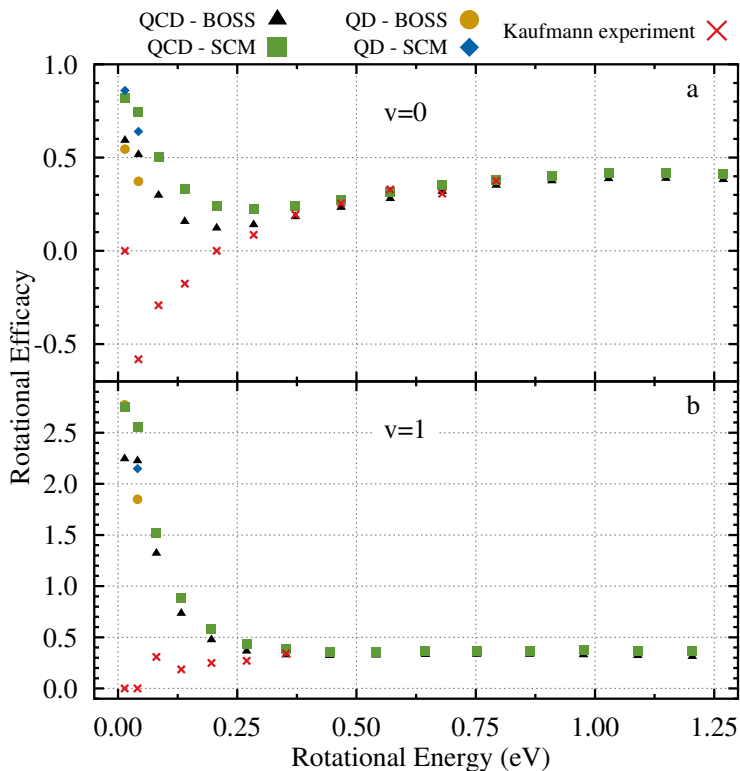
FIGURE 6.7: Rotational efficacies obtained for the QD-SCM (blue), QCD-SCM (green), QD-BOSS (orange), and QCD-BOSS (black) dissociation curves. Data are included for the (a) v=0 and (b) v=1 vibrational states, plotted against the rotational energy of the H_2 molecule. Rotational energies are obtained from the FGH method for the SRP48 PES, calculated using Eq. 2.75. Where available, the experimental results of Kaufmann *et al.*[7] are also included.

TABLE 6.1: Vibrational efficacies for the QD-SCM, QCD-SCM, QD-BOSS, and QCD-BOSS approaches, as well as the experimental results of Kaufmann *et al.*[7], calculated using Eq. 2.76.

	QD		QCD		Experiment
	BOSS	SCM	BOSS	SCM	
μ_{vib}	0.593	0.645	0.560	0.595	0.636

well as experimental results all show a rotational efficacy of around 0.40 at higher rotational states, with the SCM efficacies perhaps ever so slightly higher. Again, we do see a good agreement between the QD and QCD results, but the limited amount of QD states sampled makes it difficult to draw any definitive conclusions.

The vibrational efficacies we find, as presented in Table 6.1, agree well with each other and the experimental results. The QD results are generally slightly higher than those of the QCD, opposite to what we find for μ_{rot}. However, we do again find slightly higher efficacies for the SCM results, compared to BOSS. Thus our model predicts that the surface distortions allow for a more efficient use of vibrational, as well as rotational, energy to pass the dissociation barrier of the surface. This can, at least partially, be explained by the large number of different potential energy landscapes we investigate when applying the SCM and its large number of different surface configurations. Nevertheless, it is likely that energetic effects also play a role.

6.3.5   Rotational quadrupole alignment parameter

Finally, we will discuss another way of looking at the effect of the internal orientation of the molecule on the reaction: the rotational quadrupole alignment parameter (RQAP). This parameter describes the molecule's "preference" of reacting either initially rotating normal to the surface (cartwheel) for negative values, or parallel to the surface (helicopter) for positive values. At exactly 0 we find no preference for either. Previous studies have also calculated this parameter using QD methods for H_2/D_2 on perfect crystal Cu(111)[22, 58, 63, 64], Cu(100)[65] and Cu(211)[66] surfaces. Similarly, a previous study has already shown that the SCM can predict these RQAPs for the $D_2/Cu(111)$ system, although this was only checked at a QC level[19]. However, to our knowledge, RQAPs computed using both QCD and QD including surface temperature effects have never been compared to each other directly, especially obtained using the same potential and based on the same underlying (SRP-DFT) functional. Yet they are of special interest for our methods, as surface
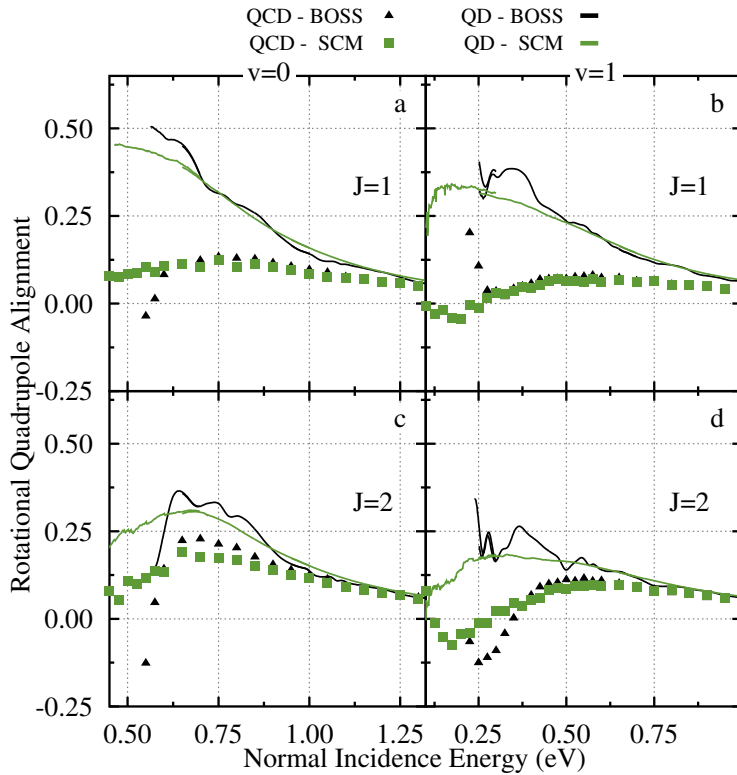
FIGURE 6.8: Rotational quadrupole alignment parameters obtained for the SCM (green curves and squares) and the BOSS (black curves and triangles) approaches for the v = 0; J = 1, J = 2 [(a) and (c)] and the v = 1; J = 1, J = 2 [(b) and (d)] rovibrational states. QD results are shown as curves, while QCD results are included as symbols (squares and triangles), calculated using Eq. 6.3.
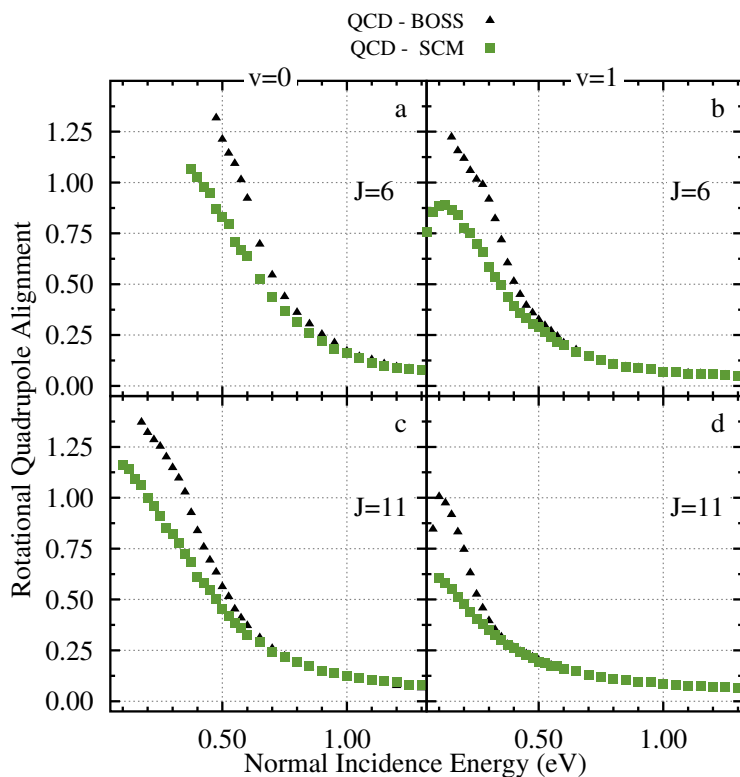
FIGURE 6.9: Rotational quadrupole alignment parameters obtained for the SCM (green squares) and the BOSS (black triangles) approaches for the v = 0; J = 6, J = 11 [(a) and (c)] and the v = 1; J = 6, J = 11 [(b) and (d)] rovibrational states. The parameters are calculated using Eq. 6.3.

temperature effects have previously been shown to clearly affect their values[19, 58]. RQAPs, as shown in figures 6.8 and 6.9, were only computed for those incidence energies with a reaction probability higher than 1%, with the QD-SCM results per surface only included in the average above this same value. Especially for the QD-SCM this greatly reduced the noise at very low energy, but did not affect the qualitative shape of the curves.

In general, we find that the QD simulations predict much higher RQAPs than the QCD results, both for the BOSS and the SCM approaches. A smaller effect was previously also observed for these states [64]. It is not immediately clear why these QD alignment parameters are much higher. One could argue that QCD allows for a much simpler redistribution of the internal rovibrational energies during dynamics, when compared to the QD simulations, which makes it easier to promote reaction even when the initial state is not favourable. Interestingly, in the case of higher rotational states, where there are a lot more states available, this effect appears to be mostly gone (Fig. 6.9) For these higher rotational states, no QD simulations were available for comparison.

For almost every curve, the highest alignments are not found at the lowest energy we include, instead only slightly behind these lowest barriers. This would then imply at least some of the lowest reaction barriers show less of a preference for rotation parallel to the surface. However, lower incidence energies also allow the molecule more time to favourably align itself to more easily surpass the reaction barriers, as the RQAPs are only determined using the initial rovibrational state in the gas phase. Furthermore, the location of the (energetically) available barriers could equally affect the amount of dynamical effects, such as rotational enhancement, that dominate for the different incidence energies. Indeed, for some rovibrational states we even find negative RQAPs at low energy, implying a preference for more "cartwheel"-like rotation. No clear difference is found between the BOSS and SCM results at these lower rotational states, although especially the QD curves do show the BOSS to predict somewhat higher alignment parameters near the peak of the curves. This difference becomes much more apparent at higher J-states, as was observed in previous work[19]. This effect can be well explained by the distorted surface configurations modifying the reaction barriers to be less ideal for the "helicopter"-like rotation, as the surface atoms are displaced in Z towards (or away) from the incoming reactant[58].

6.4 Conclusion

We have presented our deeper analysis of the previously published 6D quantum dynamical and quasi-classical results of H_2 dissociating on a thermally distorted

Cu(111) surface using the static corrugation model. As was suggested in the previous study, we show that the upturn in reaction probability we find at very low incidence energies, both for QD-BOSS and -SCM, can be entirely removed by propagating the 6D WPs with a smaller time step. Additional analysis with the flux analysis method similarly showed the upturn to not be explained by parts of the wavepackets passing past the reaction barrier in large r (H↔H) ranges.

We show how the thermal distortion of the Cu(111) surface also leads to changes in not only the barrier height, but also the barrier location and the shape of the reaction channel, when considering the H$_2$ dissociation, with the lowest reaction barrier moving toward slightly higher r and lower Z values.

Expanding the available QD results with several higher energy WPs, the dissociation curves obtained from theory were fitted to several sigmoidal functions, which were used to simulate time-of-flight spectra. We found improved agreement between the spectra available from the state-of-the-art desorption experiments and our (QD-)SCM approach when describing the H$_2$ dissociation reaction. The fitted parameters of the ERF sigmoidal function also showed a clear effect of curve broadening when surface temperature is included in the model, as well as small surface temperature effects. These smaller effects could be well explained by changes in both barrier height and location, due to the thermal surface distortions.

Next we calculated a threshold offset parameter for our results, which describes the energy shift required for a curve at a higher internal energy to match that of the rovibrational ground state. These parameters were used to calculate the rotational and vibrational efficacies of our models, which were compared those to the values found in experiments. As expected, our theoretical results reproduced experiment well for these parameters, although the overall effect of surface temperature on these parameters appeared to be very minor. Only for very low rotational energies did we find differences compared to experiment, where the rotational efficacy is predicted to be negative, which is not reproduced by any of our theoretical approaches.

Finally, we also computed rotational quadrupole alignment parameters to analyse the impact of the different rotational states on the reaction from another angle. Here we found a much larger preference for the incoming H$_2$ to react with a rotation parallel to the surface when using our QD methods, compared to the QCD methods.

Overall, this work present a wide database of experimentally obtainable parameters that can be used to validate the quality of our current and other theoretical and experimental works, when looking at the H$_2$ on Cu(111) dissociation reaction.

6.A Appendix: Additional computational details

TABLE 6.A.1: Computational details for the TDWP quantum dynamics simulations of H_2 dissociation on a Cu(111) surface.

	0.10-0.30 eV	0.25-0.70 eV
Z_{start} (a_0)	-1.0	-1.0
$N_{Z_{spec}}$	180	256
N_Z	128	180
ΔZ (a_0)	0.15	0.15
Z_{ana} (a_0)	9.20	12.05
R_{start} (a_0)	0.60	0.60
N_r	64	64
ΔR (a_0)	0.15	0.15
N_x	24	24
N_y	24	24
Max. J in basis set	18	18
Max. m_J in basis set	12	12
SCM cutoff (a_0)	16.0	16.0
Complex absorbing potentials		
Z^{CAP} start (a_0)	9.35	12.20
Z^{CAP} end (a_0)	18.05	25.85
Z^{CAP} optimum (eV)	0.05	0.125
Z^{CAP}_{spec} start (a_0)	17.00	31.95
Z^{CAP}_{spec} end (a_0)	25.85	37.25
Z^{CAP}_{spec} optimum (eV)	0.05	0.125
R^{CAP} start (a_0)	4.20	4.20
R^{CAP} end (a_0)	10.05	10.05
R^{CAP} optimum (eV)	0.10	0.10
Propagation		
Δt ($\hbar/E_h$)	1.5	2.5
t_f ($\hbar/E_h$)	60000	45000
Initial wave packet		
E_{min} (eV)	0.10	0.25
E_{max} (eV)	0.30	0.70
Z_0 (a_0)	13.10	21.95

6

TABLE 6.A.2: Additional computational details for the TDWP quantum dynamics simulations of H_2 dissociation on a Cu(111) surface.

	0.65-1.00 eV	0.95-1.50 eV
Z_{start} (a$_0$)	-1.0	-1.0
$N_{Z_{spec}}$	256	256
N_Z	180	180
ΔZ (a$_0$)	0.15	0.12
Z_{ana} (a$_0$)	12.05	12.08
R_{start} (a$_0$)	0.60	0.60
N_r	64	64
ΔR (a$_0$)	0.15	0.15
N_x	24	24
N_y	24	24
Max. J in basis set	18	18
Max. m$_J$ in basis set	12	12
SCM cutoff (a$_0$)	16.0	16.0
Complex absorbing potentials		
Z^{CAP} start (a$_0$)	12.20	12.20
Z^{CAP} end (a$_0$)	25.85	20.48
Z^{CAP} optimum (eV)	0.325	0.475
Z^{CAP}_{spec} start (a$_0$)	31.95	21.68
Z^{CAP}_{spec} end (a$_0$)	37.25	29.60
Z^{CAP}_{spec} optimum (eV)	0.325	0.475
R^{CAP} start (a$_0$)	4.20	4.20
R^{CAP} end (a$_0$)	10.05	10.05
R^{CAP} optimum (eV)	0.10	0.10
Propagation		
Δt ($\hbar/E_h$)	2.5	2.5
t_f ($\hbar/E_h$)	45000	45000
Initial wave packet		
E_{min} (eV)	0.65	0.95
E_{max} (eV)	1.00	1.50
Z_0 (a$_0$)	21.95	16.88

TABLE 6.A.3: Additional computational details for the TDWP quantum dynamics simulations of H_2 dissociation on a Cu(111) surface.

	Low time step	Flux analysis
Z_{start} (a_0)	-1.0	-1.0
$N_{Z_{spec}}$	512	512
N_Z	180	180
ΔZ (a_0)	0.15	0.15
Z_{ana} (a_0)	15.20	15.20
R_{flux} (a_0)	3.85	3.85
R_{start} (a_0)	0.40	0.40
N_r	64	64
ΔR (a_0)	0.15	0.15
N_x	16	16
N_y	16	16
Max. J in basis set	12	12
Max. m_J in basis set	8	8
Complex absorbing potentials		
Z^{CAP} start (a_0)	15.20	12.20
Z^{CAP} end (a_0)	25.85	25.85
Z^{CAP} optimum (eV)	0.05	0.05
Z^{CAP}_{spec} start (a_0)	36.80	36.80
Z^{CAP}_{spec} end (a_0)	75.65	75.65
Z^{CAP}_{spec} optimum (eV)	0.05	0.05
R^{CAP} start (a_0)	4.30	4.30
R^{CAP} end (a_0)	8.20	8.20
R^{CAP} optimum (eV)	0.10	0.10
Propagation		
Δt ($\hbar/E_h$)	0.1	2.0
t_f ($\hbar/E_h$)	180000	180000
Initial wave packet		
E_{min} (eV)	0.10	0.10
E_{max} (eV)	0.30	0.30
Z_0 (a_0)	26.0	26.0

References

(1) Berger, H. F.; Leisch, M.; Winkler, A.; Rendulic, K. D. A Search for Vibrational Contributions to the Activated Adsorption of H_2 on Copper. *Chemical Physics Letters* **1990**, *175*, 425–428, DOI: 10.1016/0009-2614(90)85558-T.

(2) Michelsen, H. A.; Rettner, C. T.; Auerbach, D. J.; Zare, R. N. Effect of rotation on the translational and vibrational energy dependence of the dissociative adsorption of D_2 on Cu(111). *The Journal of Chemical Physics* **1993**, *98*, 8294–8307, DOI: 10.1063/1.464535.

(3) Rettner, C. T.; Michelsen, H. A.; Auerbach, D. J. Quantum-state-specific dynamics of the dissociative adsorption and associative desorption of H_2 at a Cu(111) surface. *The Journal of Chemical Physics* **1995**, *102*, 4625–4641, DOI: 10.1063/1.469511.

(4) Hodgson, A.; Samson, P.; Wight, A.; Cottrell, C. Rotational Excitation and Vibrational Relaxation of H_2 Scattered from Cu(111). *Physical Review Letters* **1997**, *78*, 963–966, DOI: 10.1103/PhysRevLett.78.963.

(5) Hou, H.; Gulding, S. J.; Rettner, C. T.; Wodtke, A. M.; Auerbach, D. J. The Stereodynamics of a Gas-Surface Reaction. *Science* **1997**, *277*, 80–82, DOI: 10.1126/science.277.5322.80.

(6) Murphy, M. J.; Hodgson, A. Adsorption and desorption dynamics of H_2 and D_2 on Cu(111): The role of surface temperature and evidence for corrugation of the dissociation barrier. *The Journal of Chemical Physics* **1998**, *108*, 4199–4211, DOI: 10.1063/1.475818.

(7) Kaufmann, S.; Shuai, Q.; Auerbach, D. J.; Schwarzer, D.; Wodtke, A. M. Associative desorption of hydrogen isotopologues from copper surfaces: Characterization of two reaction mechanisms. *The Journal of Chemical Physics* **2018**, *148*, 194703, DOI: 10.1063/1.5025666.

(8) Chadwick, H.; Somers, M. F.; Stewart, A. C.; Alkoby, Y.; Carter, T. J. D.; Butkovicova, D.; Alexandrowicz, G. Stopping Molecular Rotation Using Coherent Ultra-Low-Energy Magnetic Manipulations. *Nature Communications* **2022**, *13*, 2287, DOI: 10.1038/s41467-022-29830-3.

(9) Díaz, C.; Pijper, E.; Olsen, R. A.; Busnengo, H. F.; Auerbach, D. J.; Kroes, G. J. Chemically accurate simulation of a prototypical surface reaction: H_2 dissociation on Cu(111). *Science (New York, N.Y.)* **2009**, *326*, 832–834, DOI: 10.1126/science.1178722.

(10)   Zhu, L.; Zhang, Y.; Zhang, L.; Zhou, X.; Jiang, B. Unified and transferable description of dynamics of H_2 dissociative adsorption on multiple copper surfaces *via* machine learning. *Physical Chemistry Chemical Physics* **2020**, *22*, 13958–13964, DOI: 10.1039/D0CP02291H.

(11)   Galparsoro, O.; Kaufmann, S.; Auerbach, D. J.; Kandratsenka, A.; Wodtke, A. M. First Principles Rates for Surface Chemistry Employing Exact Transition State Theory: Application to Recombinative Desorption of Hydrogen from Cu(111). *Physical Chemistry Chemical Physics* **2020**, *22*, 17532–17539, DOI: 10.1039/D0CP02858D.

(12)   Smits, B.; Somers, M. F. Beyond the static corrugation model: Dynamic surfaces with the embedded atom method. *The Journal of Chemical Physics* **2021**, *154*, 074710, DOI: 10.1063/5.0036611.

(13)   Smeets, E. W. F.; Kroes, G.-J. Designing New SRP Density Functionals Including Non-Local vdW-DF2 Correlation for H_2 + Cu(111) and Their Transferability to H_2 + Ag(111), Au(111) and Pt(111). *Physical Chemistry Chemical Physics* **2021**, *23*, 7875–7901, DOI: 10.1039/D0CP05173J.

(14)   Smeets, E. W. F.; Kroes, G.-J. Performance of Made Simple Meta-GGA Functionals with rVV10 Nonlocal Correlation for H_2 + Cu(111), D_2 + Ag(111), H_2 + Au(111), and D_2 + Pt(111). *The Journal of Physical Chemistry C* **2021**, *125*, 8993–9010, DOI: 10.1021/acs.jpcc.0c11034.

(15)   Smits, B.; Litjens, L. G. B.; Somers, M. F. Accurate Description of the Quantum Dynamical Surface Temperature Effects on the Dissociative Chemisorption of H_2 from Cu(111). *The Journal of Chemical Physics* **2022**, *156*, 214706, DOI: 10.1063/5.0094985.

(16)   Smits, B.; Somers, M. F. The Quantum Dynamics of H_2 on Cu(111) at a Surface Temperature of 925 K: Comparing State-of-the-Art Theory to State-of-the-Art Experiments. *The Journal of Chemical Physics* **2022**, *157*, 134704, DOI: 10.1063/5.0112036.

(17)   Díaz, C.; Olsen, R. A.; Auerbach, D. J.; Kroes, G. J. Six-Dimensional Dynamics Study of Reactive and Non Reactive Scattering of H_2 from Cu(111) Using a Chemically Accurate Potential Energy Surface. *Physical Chemistry Chemical Physics* **2010**, *12*, 6499–6519, DOI: 10.1039/C0019 56A.

(18)   Bonfanti, M.; Díaz, C.; Somers, M. F.; Kroes, G.-J. Hydrogen Dissociation on Cu(111): The Influence of Lattice Motion. Part I. *Physical Chemistry Chemical Physics* **2011**, *13*, 4552, DOI: 10.1039/c0cp01746a.

6

(19)   Wijzenbroek, M.; Somers, M. F. Static surface temperature effects on the dissociation of H$_2$ and D$_2$ on Cu(111). *The Journal of Chemical Physics* **2012**, *137*, 054703, DOI: 10.1063/1.4738956.

(20)   Nattino, F.; Genova, A.; Guijt, M.; Muzas, A. S.; Díaz, C.; Auerbach, D. J.; Kroes, G.-J. Dissociation and recombination of D$_2$ on Cu(111): ab initio molecular dynamics calculations and improved analysis of desorption experiments. *The Journal of Chemical Physics* **2014**, *141*, 124705, DOI: 10.1063/1.4896058.

(21)   Bonfanti, M.; Somers, M. F.; Díaz, C.; Busnengo, H. F.; Kroes, G.-J. 7D Quantum Dynamics of H$_2$ Scattering from Cu(111): The Accuracy of the Phonon Sudden Approximation. *Zeitschrift für Physikalische Chemie* **2013**, 130617035227002, DOI: 10.1524/zpch.2013.0405.

(22)   Mondal, A.; Wijzenbroek, M.; Bonfanti, M.; Díaz, C.; Kroes, G.-J. Thermal Lattice Expansion Effect on Reactive Scattering of H$_2$ from Cu(111) at T$_s$ = 925 K. *The Journal of Physical Chemistry A* **2013**, *117*, 8770–8781, DOI: 10.1021/jp4042183.

(23)   Kroes, G.-J.; Juaristi, J. I.; Alducin, M. Vibrational Excitation of H$_2$ Scattering from Cu(111): Effects of Surface Temperature and of Allowing Energy Exchange with the Surface. *The Journal of Physical Chemistry C* **2017**, *121*, 13617–13633, DOI: 10.1021/acs.jpcc.7b01096.

(24)   Spiering, P.; Wijzenbroek, M.; Somers, M. F. An improved static corrugation model. *The Journal of Chemical Physics* **2018**, *149*, 234702, DOI: 10.1063/1.5058271.

(25)   Smith, C.; Hill, A. K.; Torrente-Murciano, L. Current and future role of Haber–Bosch ammonia in a carbon-free energy landscape. *Energy & Environmental Science* **2020**, *13*, 331–344, DOI: 10.1039/C9EE02873K.

(26)   Chorkendorff, I., *Concepts of Modern Catalysis and Kinetics*; Wiley-VCH: Weinheim, 2003.

(27)   Kroes, G.-J.; Díaz, C. Quantum and classical dynamics of reactive scattering of H$_2$ from metal surfaces. *Chemical Society Reviews* **2016**, *45*, 3658–3700, DOI: 10.1039/c5cs00336a.

(28)   Kroes, G.-J. Computational approaches to dissociative chemisorption on metals: towards chemical accuracy. *Physical Chemistry Chemical Physics* **2021**, *23*, 8962–9048, DOI: 10.1039/D1CP00044F.

(29) Xiao, Y.; Dong, W.; Busnengo, H. F. Reactive force fields for surface chemical reactions: A case study with hydrogen dissociation on Pd surfaces. *The Journal of Chemical Physics* **2010**, *132*, 014704, DOI: 10.1063/1.3265854.

(30) Lozano, A.; Shen, X. J.; Moiraghi, R.; Dong, W.; Busnengo, H. F. Cutting a chemical bond with demon's scissors: Mode- and bond-selective reactivity of methane on metal surfaces. *Surface Science* **2015**, *640*, 25–35, DOI: 10.1016/j.susc.2015.04.002.

(31) Seminara, G. N.; Peludhero, I. F.; Dong, W.; Martínez, A. E.; Busnengo, H. F. Molecular Dynamics Study of Molecular and Dissociative Adsorption Using System-Specific Force Fields Based on Ab Initio Calculations: CO/Cu(110) and CH$_4$/Pt(110). *Topics in Catalysis* **2019**, *62*, 1044–1052, DOI: 10.1007/s11244-019-01196-9.

(32) Tiwari, A. K.; Nave, S.; Jackson, B. The temperature dependence of methane dissociation on Ni(111) and Pt(111): Mixed quantum-classical studies of the lattice response. *The Journal of Chemical Physics* **2010**, *132*, 134702, DOI: 10.1063/1.3357415.

(33) Guo, H.; Farjamnia, A.; Jackson, B. Effects of Lattice Motion on Dissociative Chemisorption: Toward a Rigorous Comparison of Theory with Molecular Beam Experiments. *The Journal of Physical Chemistry Letters* **2016**, *7*, 4576–4584, DOI: 10.1021/acs.jpclett.6b01948.

(34) Jackson, B. The Trapping of Methane on Ir(111): A First-Principles Quantum Study. *The Journal of Chemical Physics* **2021**, *155*, 044705, DOI: 10.1063/5.0058672.

(35) Jackson, B. Quantum studies of methane-metal inelastic diffraction and trapping: The variation with molecular orientation and phonon coupling. *Chemical Physics* **2022**, *559*, 111516, DOI: 10.1016/j.chemphys.2022.111516.

(36) Kroes, G. J.; Wijzenbroek, M.; Manson, J. R. Possible effect of static surface disorder on diffractive scattering of H$_2$ from Ru(0001): Comparison between theory and experiment. *The Journal of Chemical Physics* **2017**, *147*, 244705, DOI: 10.1063/1.5011741.

(37) Dutta, J.; Mandal, S.; Adhikari, S.; Spiering, P.; Meyer, J.; Somers, M. F. Effect of surface temperature on quantum dynamics of H$_2$ on Cu(111) using a chemically accurate potential energy surface. *The Journal of Chemical Physics* **2021**, *154*, 104103, DOI: 10.1063/5.0035830.

6

166

Chapter 6. The quantum dynamics of H_2 on Cu(111) at a surface temperature of 925 K: Comparing theory to experiments 2

(38) Dutta, J.; Naskar, K.; Adhikari, S.; Spiering, P.; Meyer, J.; Somers, M. F. Effect of surface temperature on quantum dynamics of D_2 on Cu(111) using a chemically accurate potential energy surface, To Be Submitted, 2022, submitted.

(39) Craig, I. R.; Manolopoulos, D. E. Quantum Statistics and Classical Mechanics: Real Time Correlation Functions from Ring Polymer Molecular Dynamics. *The Journal of Chemical Physics* **2004**, *121*, 3368–3373, DOI: 10.1063/1.1777575.

(40) Suleimanov, Y. V.; Aoiz, F. J.; Guo, H. Chemical Reaction Rate Coefficients from Ring Polymer Molecular Dynamics: Theory and Practical Applications. *The Journal of Physical Chemistry A* **2016**, *120*, 8488–8502, DOI: 10.1021/acs.jpca.6b07140.

(41) Behler, J. First Principles Neural Network Potentials for Reactive Simulations of Large Molecular and Condensed Systems. *Angewandte Chemie International Edition* **2017**, *56*, 12828–12840, DOI: https://doi.org/10.1002/anie.201703114.

(42) Artrith, N.; Behler, J. High-dimensional neural network potentials for metal surfaces: A prototype study for copper. *Physical Review B* **2012**, *85*, 045439, DOI: 10.1103/PhysRevB.85.045439.

(43) Lin, Q.; Zhang, L.; Zhang, Y.; Jiang, B. Searching Configurations in Uncertainty Space: Active Learning of High-Dimensional Neural Network Reactive Potentials. *Journal of Chemical Theory and Computation* **2021**, *17*, 2691–2701, DOI: 10.1021/acs.jctc.1c00166.

(44) Olsen, R. A.; Kroes, G. J.; Lo/vvik, O. M.; Baerends, E. J. The Influence of Surface Motion on the Direct Subsurface Absorption of H_2 on Pd(111). *The Journal of Chemical Physics* **1997**, *107*, 10652–10661, DOI: 10.1063/1.474181.

(45) Kroes, G.-J.; Somers, M. F. Six-dimensional dynamics of dissociative chemisorption of H_2 on metal surfaces. *Journal of Theoretical and Computational Chemistry* **2005**, *04*, 493–581, DOI: 10.1142/S0219633605001647.

(46) Chadwick, H.; Alkoby, Y.; Cantin, J. T.; Lindebaum, D.; Godsi, O.; Maniv, T.; Alexandrowicz, G. Molecular spin echoes; multiple magnetic coherences in molecule surface scattering experiments. *Physical Chemistry Chemical Physics* **2021**, *23*, 7673–7681, DOI: 10.1039/D0CP05399F.

(47) Vibok, A.; Balint-Kurti, G. G. Parametrization of complex absorbing potentials for time-dependent quantum dynamics. *The Journal of Physical Chemistry* **1992**, *96*, 8712–8719, DOI: `10.1021/j100201a012`.

(48) Balint-Kurti, G. G.; Dixon, R. N.; Marston, C. C. Grid methods for solving the Schrödinger equation and time dependent quantum dynamics of molecular photofragmentation and reactive scattering processes. *International Reviews in Physical Chemistry* **1992**, *11*, 317–344, DOI: `10.1080/01442359209353274`.

(49) Neuhauser, D.; Baer, M.; Judson, R. S.; Kouri, D. J. The Application of Time-Dependent Wavepacket Methods to Reactive Scattering. *Computer Physics Communications* **1991**, *63*, 460–481, DOI: `10.1016/0010-4655(91)90270-U`.

(50) Zhang, D. H.; Zhang, J. Z. H. Full-dimensional Time-dependent Treatment for Diatom–Diatom Reactions: The H_2+OH Reaction. *The Journal of Chemical Physics* **1994**, *101*, 1146–1156, DOI: `10.1063/1.467808`.

(51) Gulding, S. J.; Wodtke, A. M.; Hou, H.; Rettner, C. T.; Michelsen, H. A.; Auerbach, D. J. Alignment of $D_2(v, J)$ Desorbed from Cu(111): Low Sensitivity of Activated Dissociative Chemisorption to Approach Geometry. *The Journal of Chemical Physics* **1996**, *105*, 9702–9705, DOI: `10.1063/1.472979`.

(52) Wetzig, D.; Rutkowski, M.; David, R.; Zacharias, H. Rotational Corrugation in Associative Desorption of D_2 from Cu(111). *Europhysics Letters* **1996**, *36*, 31, DOI: `10.1209/epl/i1996-00183-2`.

(53) Shuai, Q.; Kaufmann, S.; Auerbach, D. J.; Schwarzer, D.; Wodtke, A. M. Evidence for Electron–Hole Pair Excitation in the Associative Desorption of H_2 and D_2 from Au(111). *The Journal of Physical Chemistry Letters* **2017**, *8*, 1657–1663, DOI: `10.1021/acs.jpclett.7b00265`.

(54) Kroes, G. J.; Wiesenekker, G.; Baerends, E. J.; Mowrey, R. C.; Neuhauser, D. Dissociative Chemisorption of H_2 on Cu(100): A Four-dimensional Study of the Effect of Parallel Translational Motion on the Reaction Dynamics. *The Journal of Chemical Physics* **1996**, *105*, 5979–5998, DOI: `10.1063/1.472450`.

(55) Kroes, G. J.; Baerends, E. J.; Mowrey, R. C. Six-Dimensional Quantum Dynamics of Dissociative Chemisorption of ($v = 0$, $j = 0$) H_2 on Cu(100). *Physical Review Letters* **1997**, *78*, 3583–3586, DOI: `10.1103/PhysRevLett.78.3583`.

6

(56)   Leforestier, C.; Bisseling, R. H.; Cerjan, C.; Feit, M. D.; Friesner, R.; Guldberg, A.; Hammerich, A.; Jolicard, G.; Karrlein, W.; Meyer, H. .-.; Lipkin, N.; Roncero, O.; Kosloff, R. A Comparison of Different Propagation Schemes for the Time Dependent Schrödinger Equation. *Journal of Computational Physics* **1991**, *94*, 59–80, DOI: 10.1016/0021-9991(91)90137-A.

(57)   Busnengo, H. F.; Salin, A.; Dong, W. Representation of the 6D potential energy surface for a diatomic molecule near a solid surface. *The Journal of Chemical Physics* **2000**, *112*, 7641–7651, DOI: 10.1063/1.481377.

(58)   Nattino, F.; Díaz, C.; Jackson, B.; Kroes, G.-J. Effect of Surface Motion on the Rotational Quadrupole Alignment Parameter of D$_2$ Reacting on Cu(111). *Physical Review Letters* **2012**, *108*, 236104, DOI: 10.1103/PhysRevLett.108.236104.

(59)   Sheng, H. W.; Kramer, M. J.; Cadien, A.; Fujita, T.; Chen, M. W. Highly optimized embedded-atom-method potentials for fourteen fcc metals. *Physical Review B* **2011**, *83*, 134118, DOI: 10.1103/PhysRevB.83.134118.

(60)   Michelsen, H. A.; Rettner, C. T.; Auerbach, D. J. On the Influence of Surface Temperature on Adsorption and Desorption in the D$_2$/Cu(111) System. *Surface Science* **1992**, *272*, 65–72, DOI: 10.1016/0039-6028(92)91422-8.

(61)   Hand, M.; Harris, J. Recoil Effects in Surface Dissociation. *The Journal of Chemical Physics* **1990**, *92*, 7610–7617, DOI: 10.1063/1.458198.

(62)   Darling, G. R.; Holloway, S. Rotational Motion and the Dissociation of H$_2$ on Cu(111). *The Journal of Chemical Physics* **1994**, *101*, 3268–3281, DOI: 10.1063/1.467574.

(63)   Dai, J.; Light, J. C. The Steric Effect in a Full Dimensional Quantum Dynamics Simulation for the Dissociative Adsorption of H$_2$ on Cu(111). *The Journal of Chemical Physics* **1998**, *108*, 7816–7820, DOI: 10.1063/1.476217.

(64)   Díaz, C.; Olsen, R. A.; Auerbach, D. J.; Kroes, G. J. Six-dimensional dynamics study of reactive and non reactive scattering of H$_2$ from Cu(111) using a chemically accurate potential energy surface. *Physical Chemistry Chemical Physics* **2010**, *12*, 6499–6519, DOI: 10.1039/C001956A.

(65) Marashdeh, A.; Casolo, S.; Sementa, L.; Zacharias, H.; Kroes, G.-J. Surface Temperature Effects on Dissociative Chemisorption of H2 on Cu(100). *The Journal of Physical Chemistry C* **2013**, *117*, 8851–8863, DOI: 10.1021/jp401311k.

(66) Smeets, E. W. F.; Füchsel, G.; Kroes, G.-J. Quantum Dynamics of Dissociative Chemisorption of H_2 on the Stepped Cu(211) Surface. *The Journal of Physical Chemistry C* **2019**, *123*, 23049–23063, DOI: 10.1021/acs.jpcc.9b06539.

6